Beam Profiling of a Commercial Lens-Assisted Terahertz Time Domain Spectrometer

Suzanna Freer, Andrei Gorodetsky, and Miguel Navarro-Cia, *Senior Member, IEEE*

***Abstract*—To undertake THz spectroscopy and imaging, and accurately design and predict the performance of quasi-optical components, knowledge of the parameters of the beam (ideally Gaussian) emitted from a THz source is paramount. Despite its proliferation, relatively little work has been done on this in the frame of broadband THz photoconductive antennas. Using primarily pinhole scanning methods, along with stepwise angular spectrum simulations, we investigate the profile and polarization characteristics of the beam emitted by a commercial silicon-lens-integrated THz photoconductive antenna and collimated by a TPX (polymethylpentene) lens. Our study flags the limitations of the different beam profiling methods and their impact on the beam Gaussianity estimation. A non-Gaussian asymmetric beam is observed, with main lobe beam waists along x and y varying from 8.4 ± 0.7 mm and 7.7 ± 0.7 mm at 0.25 THz, to 1.4 ± 0.7 mm and 1.4 ± 0.7 mm at 1 THz, respectively. Additionally, we report a maximum cross-polar component relative to the ON-axis co-polar component of -11.6 dB and -21.2 dB, at 0.25 THz and 1 THz, respectively.**

***Index Terms*—Beam profile, edge diffraction, Gaussian beam, imaging, quasi-optics, terahertz, time-domain spectrometer.**

I. Introduction

RECENT years have witnessed a significant technological development of commercial THz instruments [1], [2], increasing the accessibility of time-domain spectroscopy (TDS). TDS enables broadband spectroscopy, providing both the temporal response and spectroscopic information of samples [2]. Additionally, TDS systems have attracted a large amount of attention regarding their imaging capabilities [3], [4]. In most imaging systems, scanning of the object with a focused THz beam is performed, which provides poor transverse spatial resolution [3].

Manuscript received June 1, 2020; revised August 19, 2020; accepted September 16, 2020. Date of publication September 24, 2020; date of current version January 5, 2021. This work was supported in part by the Engineering and Physical Sciences Research Council under Grant EP/S018395/1, in part by the Royal Society under Grant IES/R3/183131, and Grant IEC/NSFC/191104. The work of Suzanna Freer was supported by the University of Birmingham [Ph.D. Studentship UKRI under Project 2137478]. The work of Miguel Navarro-Cía was supported in part by the Royal Society under Grant RSG/R1/180040, and in part by the University of Birmingham [Birmingham Fellowship]. *(Corresponding author: Miguel Navarro-Cía.)*

Suzanna Freer and Miguel Navarro-Cia are with the School of Physics and Astronomy, University of Birmingham, Birmingham, B15 2TT, U.K. (e-mail: SXF845@student.bham.ac.uk; M.Navarro-Cia@bham.ac.uk).

Andrei Gorodetsky is with the School of Physics and Astronomy, University of Birmingham, Birmingham, B15 2TT, U.K., and also with the ITMO University, 197101 St. Petersburg, Russia (e-mail: andrei@itmo.ru).

Color versions of one or more of the figures in this article are available online at https://ieeexplore.ieee.org.

Digital Object Identifier 10.1109/TTHZ.2020.3026656

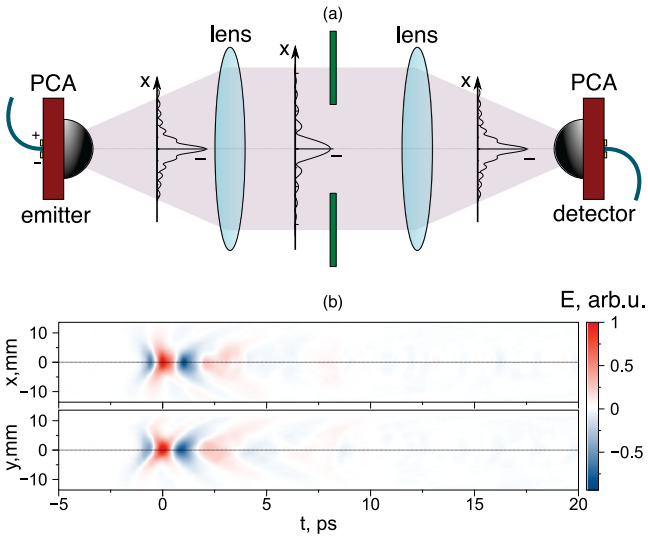

Fig. 1. (a) General optical layout of the 2f + 230 mm setup implemented with the TERA K15 THz TDS. Beam intensity profiles at different stages are shown; PCA stands for photoconductive antenna. (b) X- and Y-time maps of the THz beam corresponding to the *pinhole-only* scan.

Alternatively, for full wavefront detection with higher spatial resolution and the ability to retrieve full spectral information with a single pixel detector, scanning with a pinhole approach can be used [5], [6]. The lack of cameras sensitive to the field produced by a TDS source with adequate resolution, in addition to the desire to avoid lengthy two-dimensional (2-D) raster scanning, has recently driven researchers towards a compressed sensing approach to single pixel detection [7], [8].

Standard THz TDS systems are comprised of an emitter and detector, both with integrated silicon lenses [2], [9]. In addition, quasi-optics [10], including lenses and mirrors, are integrated into the system to control the beam as it propagates, see Fig. 1(a). Precise knowledge of the beam parameters over the whole frequency range of the system (more than a decade for THz TDS) is fundamental for spectroscopy [11], [12] and imaging [4]. This includes not only the beam waist (i.e., 1/e decay half width of the field amplitude), but also its cross-polar level. Seminal work was carried out around the turn of the century in these fronts for optical free-space-coupled [13], [14], fiber coupled [15]–[17], and hybrid [18] in-house systems. Since then, beam characterization of free-space-coupled in-house systems has been undertaken [19]–[22].

Nowadays, most commercial THz TDS systems are fiber coupled to utilize the mature and cost-efficient telecom technology.

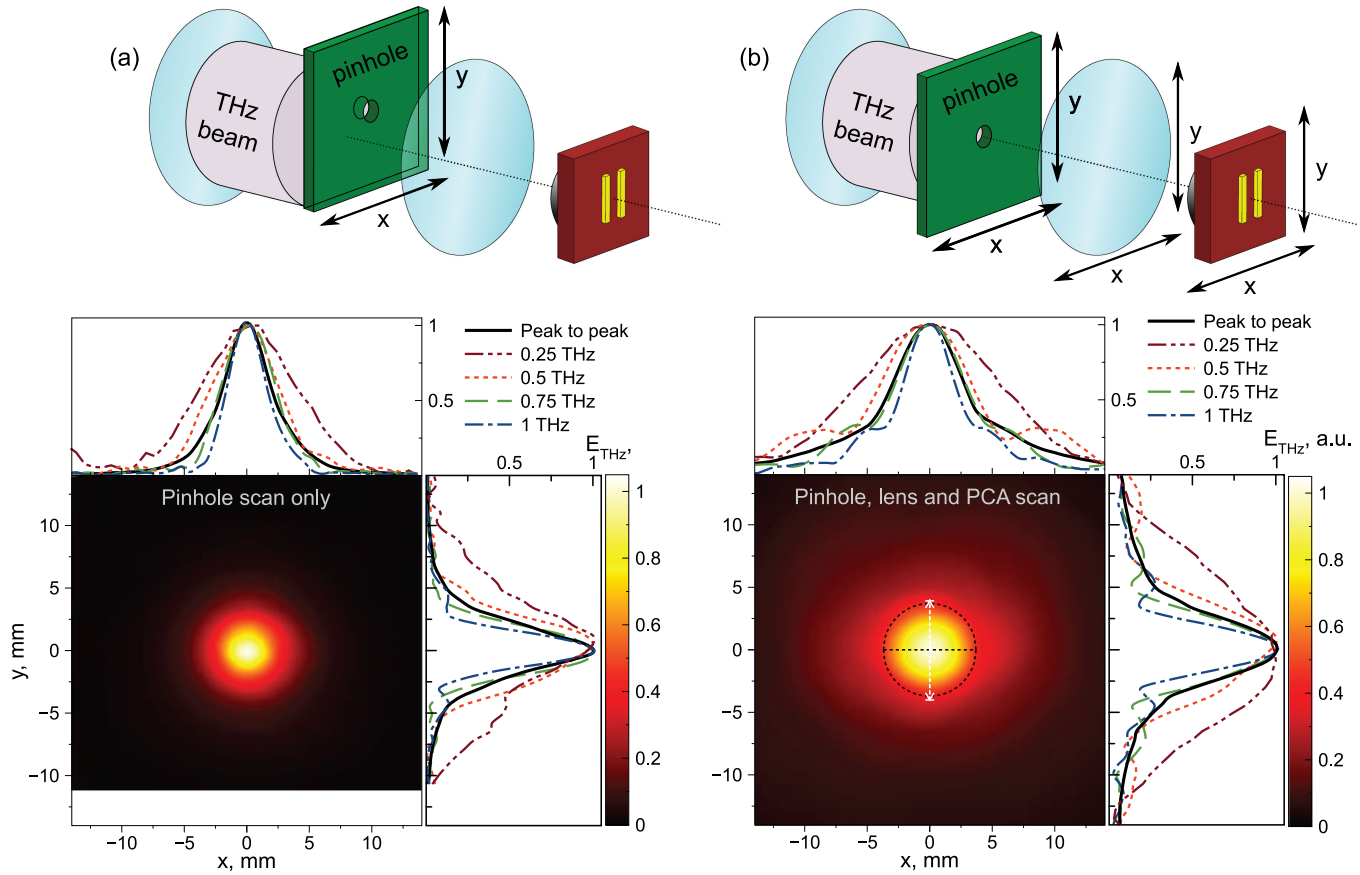

Fig. 2. Peak-to-peak THz beam profiles obtained from two different pinhole scanning approaches, whose layouts can be found in the top insets. (a) Two-dimensional raster scan of a ⌀1 mm *pinhole-only*. (b) Two-dimensional raster scan of a ⌀1 mm pinhole and detector together. The pinhole was placed in the middle point of the THz setup. The cross-section plots show the peak-to-peak profiles together with profiles at different frequencies.

The beam profiles in such systems are expected to be similar to those of free-spaced-coupled systems since the THz beam profile is a function of the photoconductive antenna, silicon lens, and any other (quasi-)optics in the emitter side, regardless of the near-infrared laser coupling mechanism. However, we will show that fiber-coupled systems enable us to de-embed the influence of the (quasi-)optics on the detector side, given the ability to scan the pinhole and detector coaligned. Such a serious consideration to the impact of the detection transfer function on the beam profiling is limited in the open literature.

Here, we compile a rigorous beam characterization of the commercial TERA K15 Mark II all fiber-coupled THz TDS system from Menlo Systems, scrutinizing the impact of the detection side (quasi-)optics on the beam profile estimate. Given the lack of commercial cameras sensitive to collimated beams from TDS systems, we report two aperture scanning methods (see Fig. 2) and a knife-edge method. The first aperture scan consists of raster scanning the pinhole. The second involves scanning the pinhole and fiber-coupled detector simultaneously, a technique which cannot be achieved in a free-space-coupled setup. This campaign of measurements is complemented by stepwise angular spectrum method results and a reduced number of computationally-affordable full-wave simulations.

II. Measurement Approaches, Results, and Initial Observations

The beam profile of a TERA K15 Mark II system is characterized here. In this system, the THz radiation is generated and detected with PCA modules manufactured by the Fraunhofer Heinrich-Hertz Institute (HHI) [23], [24]. The detailed PCA modules and system specifications as well as measurement settings are listed in Appendix A. The raw experimental data in all setups is the THz time trace (i.e., waveform). An example of such raw data can be found in Fig. 1(b). The spectral response is then obtained by Fourier transformation with Hanning windowing.

A. Pinhole-Only Scanning Method

Spatially sampling the THz beam by raster scanning a pinhole in the xy plane across the setup is the most popular method for both far-field [19] and near-field [25]–[27] beam mapping. Precautions should be taken for far-field mapping, however, as discussed in the following section. Here, the pinhole consisted of a 1 mm thick metallic plate acting as a beam block, with a small aperture. The pinhole diameter affects both the resolution of the image and signal-to-noise ratio of the detected signal. One must therefore find a compromise between the two [19].

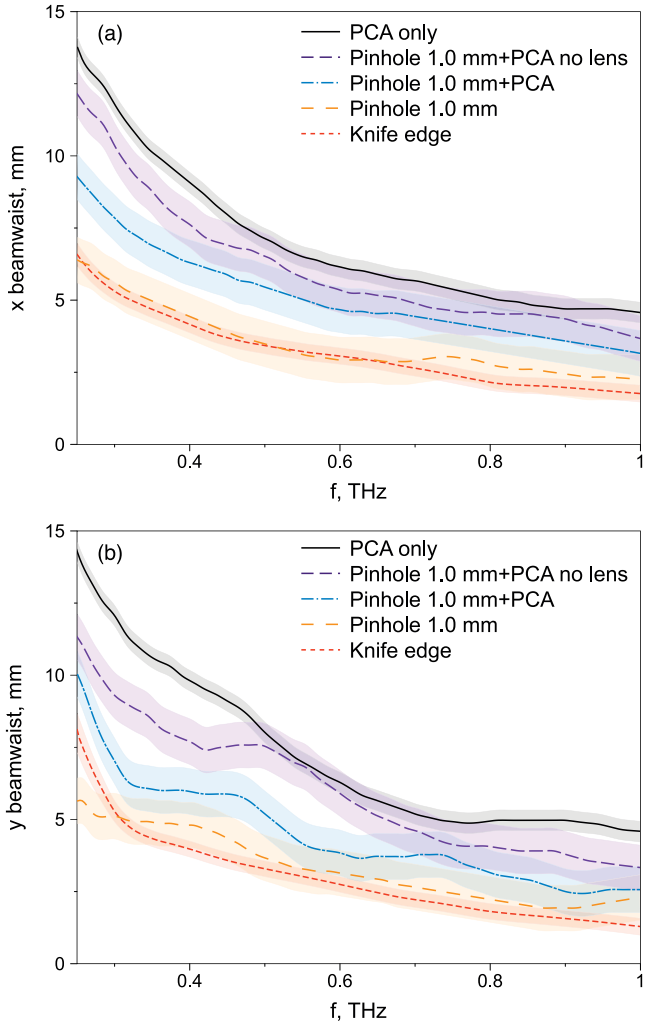

Fig. 3. Beam waist along (a) x and (b) y as a function of frequency for the five different scanning settings discussed in the manuscript: the *pinhole-only* scanning method (method A), the co-aligned *pinhole and detector* scanning method with (method B) and without focusing TPX lens (method C), the detector scanning method without focusing TPX lens (method C) and the knife-edge method (see Appendix C). The shaded regions represent uncertainty.

Here, an aperture diameter of 1 mm was chosen and kept throughout the manuscript. The raster scan step was 0.7 mm along both the $x-$ and y-axes. The distance between the two TPX lenses [see Fig. 1(b)] was approximately 230 mm, and the scanned plane corresponded to the middle plane of the THz setup. The beam waist of the main lobe, tabulated in Appendix B, was subsequently extracted from the field image presented in Fig. 2(a), see Fig. 3.

B. Pinhole and Detector Scanning Method

To determine the effect of the detection process on measurements (i.e., to de-embed the receiving pattern of the detector), the detector was scanned simultaneously with the pinhole. Two scans were undertaken: the first with the detector unit (including the TPX lens) positioned approximately 100 mm from the pinhole plane [see Fig. 2(b)]. This 15 mm offset compared to method A was introduced to enable the pinhole and detector to be mounted on the same xy-stage. For the second scan, the pinhole was moved toward the detector and positioned approximately 4 mm from the detector TPX lens [see Fig. 4(c)]. In this instance, the scanning plane did not correspond to the middle plane of the THz setup. The raster scan steps for the two methods were 0.7 mm and 0.5 mm, respectively.

From the frequency domain field cross sections in Fig. 2(b) and the extracted beam waists in Fig. 3, one can observe a narrower beam waist along the y-axis (H plane). This is corroborated by the knife-edge results in Appendix C. This asymmetry is attributed to the effect of the s- and p-polarized Fresnel reflection at the silicon lens surface in both the PCA emitter and detector. In the x (E plane) and y (H plane) directions, the field is p- and s-polarized, respectively. p-polarized light exhibits a lower reflection coefficient, resulting in higher transmission. CST Microwave Studio full-wave simulations of the lens-assisted PCA confirm the asymmetry of the beam due to the Fresnel reflection. The fact that such asymmetry is not visible in the *pinhole-only* scanning method [see Fig. 2(a)] is likely due to the reduction of the field projection in the detector plane for the OFF-axis field, i.e., the field further from the beam axis has a smaller field projection in the detector plane. Note that an asymmetric beam has also been reported for a newer generation of emitter modules from HHI [17].

The fixed frequency field cross-sections presented in Figs. 2(b) and 4(c) (measured in the central plane and the plane 4 mm from the detector) exhibit interference fringes. Given the recorded temporal window of 52 ps, these fringes are attributed to the refractive index step between the silicon lens and InP substrate of the emitter [13], [18], [20], as confirmed by our CST Microwave Studio full-wave simulations. It should be noted that these fringes do not appear in the *pinhole-only* scan images [see Fig. 2(a)]. This is possibly a result of the field projection on the detector. Hence, side-lobes become suppressed when the detector is not in-line with the pinhole axis. This finding, alongside the fact that the *pinhole-only* scanning method is the common standard, may explain the frequent reports of Gaussian beams for TDS systems [2], [9], [16], [18], [19], [21], [28], in contrast to the initial understanding [13].

Our full-wave simulations also reveal the increasing significance of the side lobes (i.e., interference fringes) when a longer temporal window is considered. This undesirable effect is due to the reflections inside the silicon lens and diffraction on the boundaries of the emitter chip. It should be of concern for spectroscopy and imaging applications requiring long time delays and CW system using these type of lens-assisted PCAs (e.g., photomixing systems) [29].

C. Removed Focusing TPX Lens Scanning Method

To determine the effect of the highly transmissive TPX lens in the detector side, the lens was removed and each scan (PCA scan without and with pinhole) were repeated, see top insets in Fig. 4(a) and (b) for layouts. A similar approach, but for a free-space-coupled system, can be found in [22]. Again, the scanning plane did not correspond to the middle plane of the THz setup used for methods A and the former B. The images

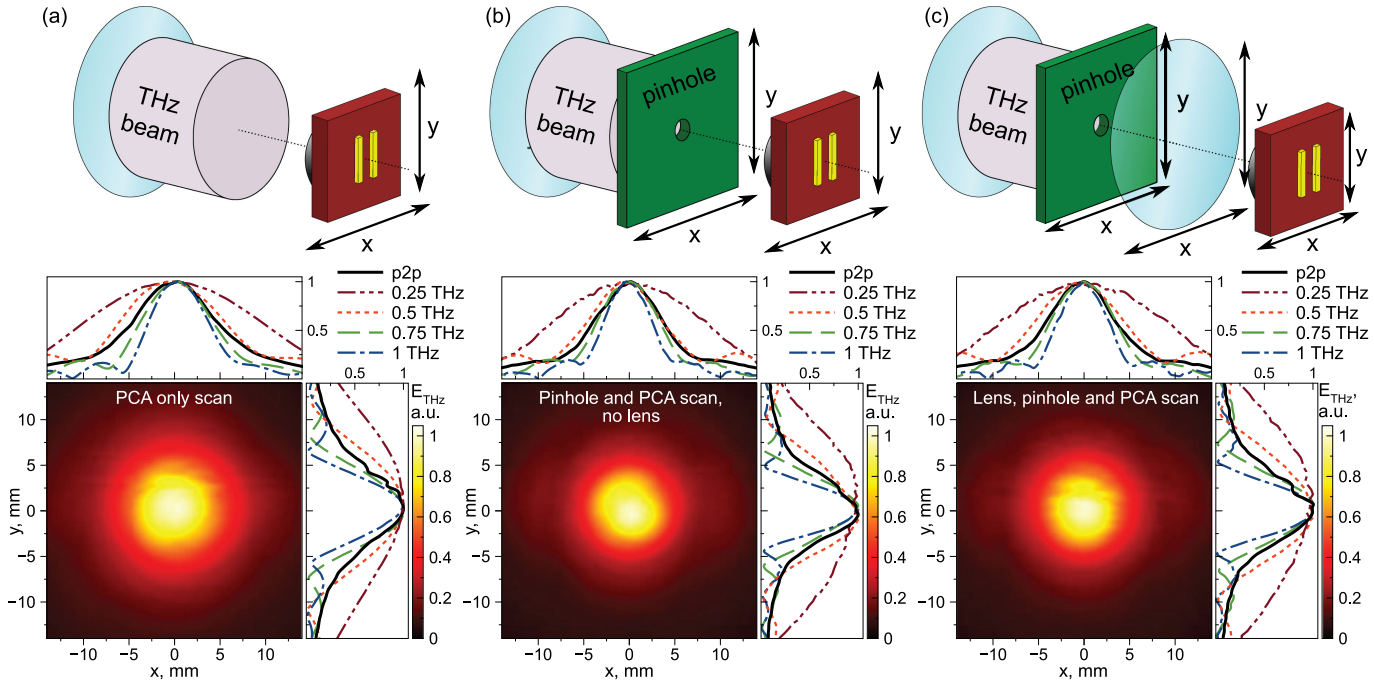

Fig. 4. Peak-to-peak THz beam profiles obtained from the three different scanning methods whose layouts can be found in the top insets. (a) Two-dimensional raster scan with the PCA only. (b) Two-dimensional raster scan with the ⌀1 mm pinhole placed at the second TPX lens position, moved together with the PCA detector. (c) Two-dimensional raster scan with the ⌀1 mm pinhole placed 4 mm in front of the second TPX lens. The cross-sectional plots show the peak-to-peak profiles together with profiles at different frequencies.

obtained are presented in Fig. 4(a) and (b). The inspection of the beam profiles for pinhole and PCA scans without and with a TPX lens presented in Fig. 4(b) and (c) confirm the negligible effect of this focusing TPX lens on the beam characterization. This, in turn, confirms that the beam in the THz setup is highly collimated, which we verified by scanning the beam at different z-planes. The residual divergence calculated from the latter measurements is $\Theta \approx 1.5^\circ$ to 0.7°, from 0.25 THz to 1 THz, in both principal planes. The corresponding beam waists as a function of frequency can be found in Fig. 3.

D. Cross-Polarized Field Distribution

The cross-polar level can be used to characterize the polarization purity of a beam. It is defined as the ratio of the cross-polar component of the field at a specific point in space to the maximum co-polar field. Despite the cross-polar level being an important characteristic for antennas [21], [30], [31], quasi-optical systems [10], [32] and spectroscopy of anisotropic materials [33], [34] and metamaterials [35]–[38], it is rarely reported for THz TDS systems, except ON-axis.

To estimate the cross-polar level in the xy plane for the *pinhole and detector* scanning method and *removed focusing TPX lens* scanning method, the detector was rotated 90° with respect to the emitter and scanned with the same translation step as the co-polar measurement counterparts. To deconvolve the detector's cross polarization from the cross-polarization measurement, the detector's polarization sensitivity was first estimated, as described in Appendix D.

The deconvolved cross-polar component in the xy plane can be seen in the second row of Figs. 5 and 6. The cross-polar measurements are a result of the combination of the emitter's cross-polarization and a diverging wave front. If one defines a vertically polarized Gaussian beam waist at a given location and propagates this beam to a plane some distance away from the optical axis, the intercepted wavefront has nonzero electric field in the horizontal electric field components. That is, a linearly, vertically polarized emitter in spherical coordinates has a nonzero E_θ component and a zero E_ϕ component. When this radiation is intercepted at a plane that is normal to $\theta = \pi/2$ and $\phi = 0$, the projection of E_θ at any point on the plane corresponding to a nonzero E_θ and a nonzero E_ϕ produces a nonzero E_x and nonzero E_y, respectively. Moreover, assuming that the $x = 0$, $y = 0$ (origin) point on the plane is coincident with the $\theta = \pi/2$, $\phi = 0$ axis, the projected horizontal electric field component should be symmetric about the x-axis and y-axis. This is in evident in Figs. 5 and 6. The abovementioned reasoning is confirmed with the calculated projections extracted from simulations using the stepwise approach to the angular spectrum method (ASM) [39]. This approach is described in more detail in Section III.

Disentangling the emitter's cross polarization and the diverging front contributions is beyond the scope of this manuscript. Nevertheless, the emitter without the collimating TPX lens has been simulated using CST Microwave Studio and its corresponding cross-polar far-field patterns for four different frequencies can be found in Appendix E. They also show the mirror symmetry about the x-axis and y-axis.

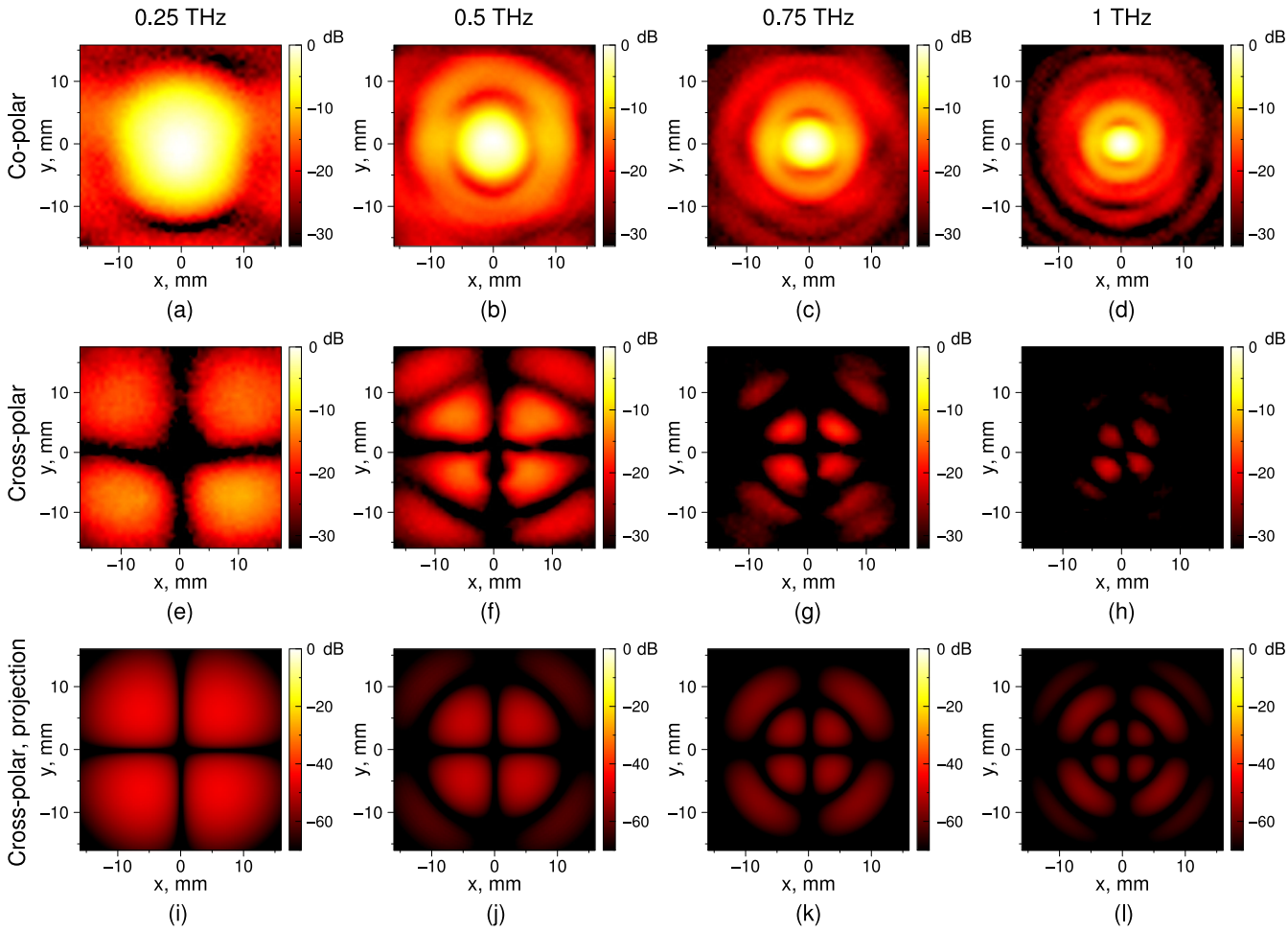

Fig. 5. Experimental co- (top row) and cross-polarization (middle row) THz beam maps at the middle plane of the THz setup for 0.25, 0.5, 0.75, and 1 THz (from left to right), obtained with the ⌀1 mm *pinhole and detector* scanning method. (Bottom row) Corresponding simulated cross-polarization THz beam maps.

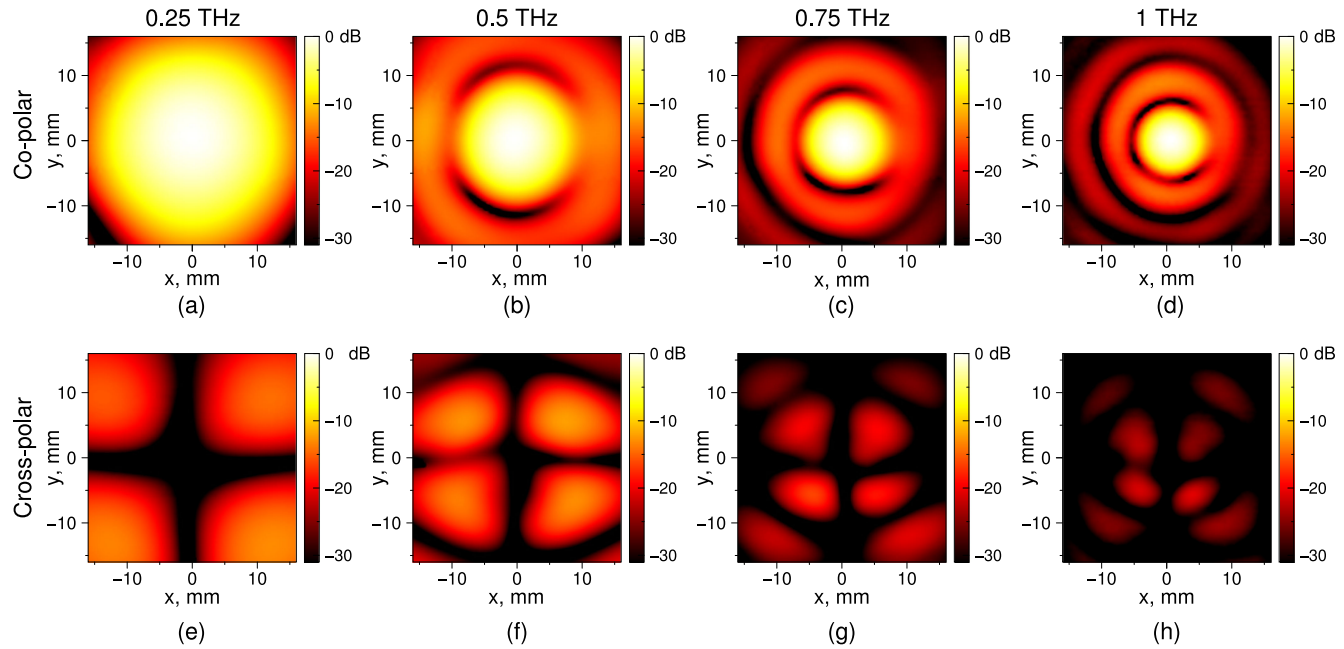

Fig. 6. Experimental co- (top row) and cross-polarization (bottom row) THz beam maps at the detector (end of the THz setup) plane for 0.25, 0.5, 0.75, and 1 THz (from left to right), obtained with the PCA only (no pinhole and no TPX lens) scanning method.

TABLE I
CROSS-POLAR LEVELS EXTRACTED FROM FIGS. 5 AND 6, FOR THE PINHOLE AND DETECTOR SCANNING METHOD AND REMOVED TPX LENS SCANNING METHOD, RESPECTIVELY

Freq, THz	Pinhole + PCA Cross-Polar Level (dB)	Removed-TPX Lens Cross-Polar Level (dB)
0.25	-11.6	-13.0
0.5	-13.9	-12.1
0.75	-17.3	-16.3
1	-21.2	-20.6

Table I presents the cross-polar levels defined as the ratio of the maximum cross-polar field to the maximum co-polar field extracted from Figs. 5 and 6. There is consistency between methods. The cross-polar levels reported here are significantly lower than that achieved in high-performance CW quasi-optical systems that provide levels of at least −30 dB [10], [32]. They are, however, better than those reported for in-house leaky lens antennas and THz PCAs [21], [31].

E. Beam Directivity

The directivity of the emitter including the collimating TPX lens was estimated using the approximated formula

$$\frac{1}{D} = \frac{1}{2}\left(\frac{1}{D_x} + \frac{1}{D_y}\right) \tag{1}$$

where D_x and D_y are the directivities extracted from the x and y cross sections [40], defined as

$$D_x = \frac{|E(\theta)|^2_{\max}}{\frac{1}{2}\int_0^{\pi} |E(\theta,0)|^2 \sin\theta d\theta} \tag{2}$$

and

$$D_y = \frac{|E(\phi)|^2_{\max}}{\frac{1}{2}\int_0^{\pi} |E(\theta,\pi/2)|^2 \sin\theta d\theta}. \tag{3}$$

$E(\theta,\phi)$ is the electric field at polar coordinates θ and ϕ. The frequency dependent directivity of the beam was calculated from the x and y cross sections of the *pinhole and detector* scan beam profile in Fig. 5. The directivity presented in Fig. 7, along with the corresponding residual divergence, show reasonable collimation of the beam. Menlo Systems data sheet reports full wave at half-maximum divergence angle of 12.5° for the emitter alone, demonstrating the good collimation provided by the TPX lens on the emitter side.

III. DISCUSSION

A. Simulation of the Beam Profile Along the System

Simulations of the beam profile along the THz setup (see Fig. 8) were performed using the stepwise approach [39] to the ASM, which is capable of simulating nonparaxial beams [41] and is often used for THz pulse propagation simulation in THz pulse time domain holography [6], [42], for example. The ASM was limited to 2-D calculation to accelerate calculation time, and was fulfilled with band limiting [43]. This assumption was made due to the axial symmetry of the system (neglecting the slight asymmetry of the emitter chip radiation pattern shown earlier). Initial beam profiles were taken as rectangular with a width of 4.22 mm, similar at all frequencies. Such initial profile produces a field distribution similar to ones reported for silicon lens coupled PCA in [13], see Fig. 9(a). The TPX lenses were accounted for in the thin lens approximation.

The characteristic frequency-dependent beam waist at the midpoint of any 4f confocal setup [44] can be seen readily in Fig. 8. These simulations confirm the non-negligible side-lobes observed in the measurements. Hence, the beam in this commercial TDS system cannot be considered Gaussian. With this caveat, we can still define a beam waist (i.e., 1/e decay

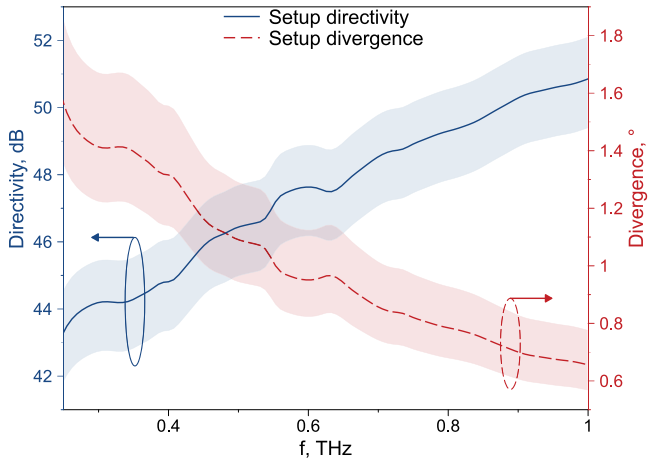

Fig. 7. THz directivity (blue solid line, left axis) and residual divergence (red dashed line, right axis) spectra, extracted from the *pinhole and detector* scan. The shaded regions represent uncertainty.

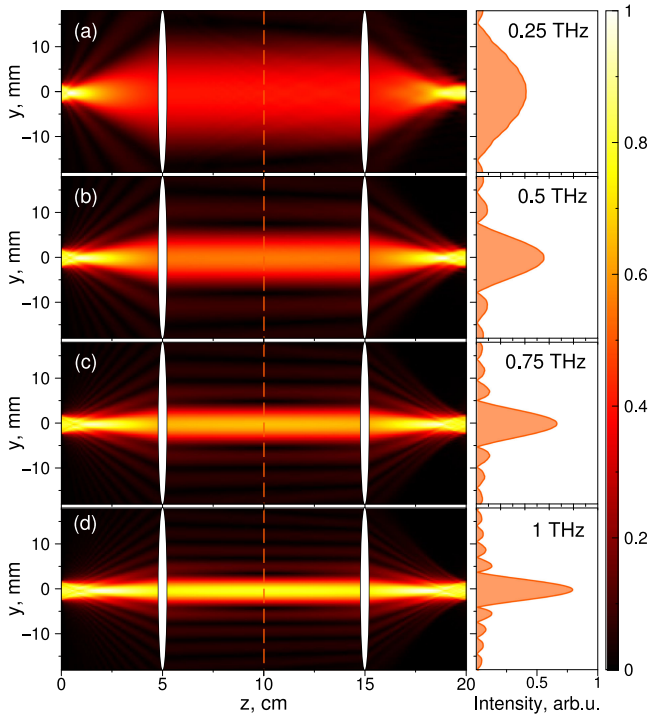

Fig. 8. Simulated normalized frequency beam profile across the setup computed via the stepwise angular spectrum method.

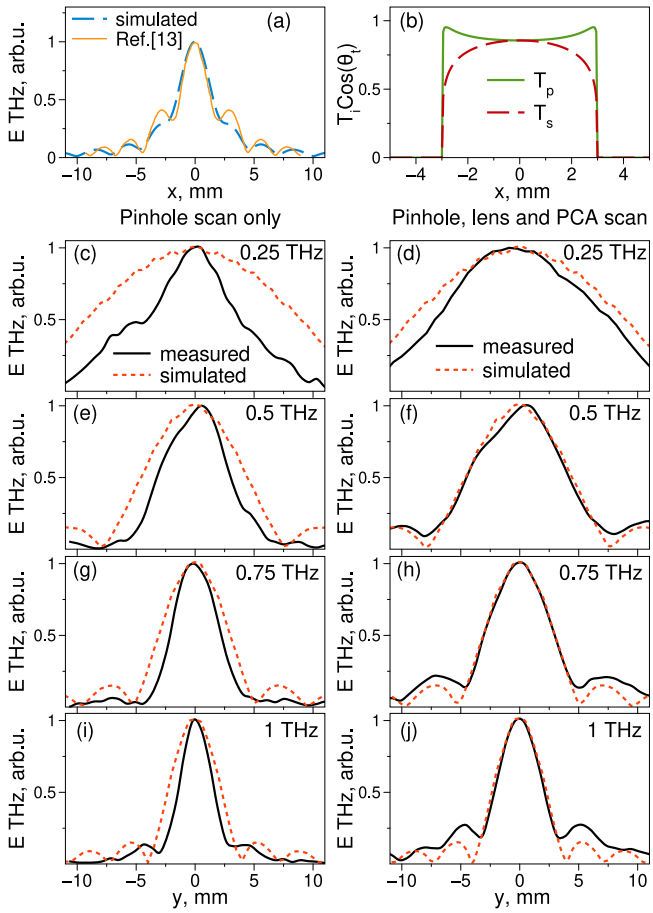

Fig. 9. (a) Simulated beam profile at 0.586 THz 25 mm from the silicon lens tip compared with the profile obtained in [13] at 0.586 THz 35 mm from the silicon lens tip. (b) PCA simulation window for s- and p-polarized radiation. (c)–(j) Beam profiles for *pinhole-only* (c), (e), (g), (i) and pinhole+lens+PCA (d), (f), (h), (j) scans. Black solid line show the experimental data for s- polarized y-axis, red curves show simulated data with scalar fields.

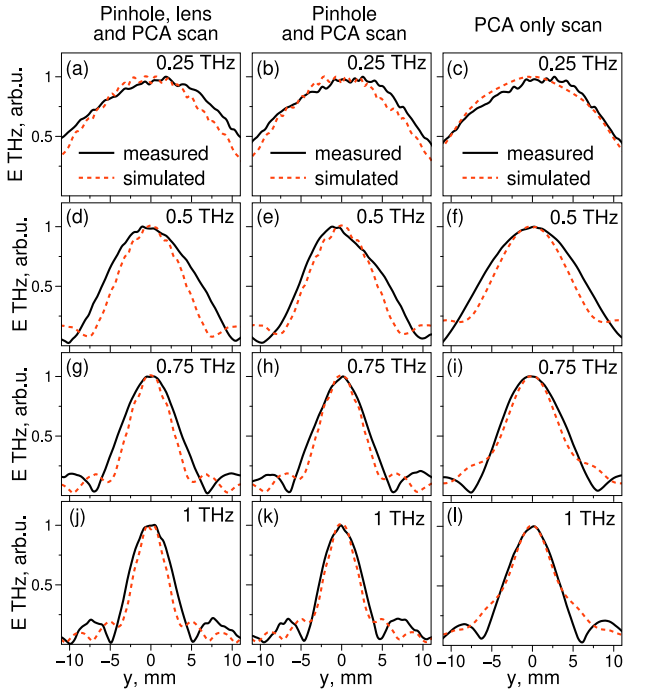

Fig. 10. Normalized beam profiles at different frequencies: 0.25 THz (a), (b), (c), 0.5 THz (d), (e), (f), 0.75 THz (g), (h), (i), 1 THz (j), (k), (l) obtained with 0.6 mm pinhole placed 4 mm in front of the second TPX lens (a), (d), (g), (j), with 0.6 mm pinhole placed instead of the second TPX lens (b), (e), (h), (k), and without a pinhole (c), (f), (j), (l). In all cases, PCA, pinhole (where present) and lens (where present) were synchronously moved.

half width of the field amplitude) for the main lobe where the Gaussian function is a good approximation [13]. Beam waists were obtained from the simulation at the midpoint of the setup (and, thus, free of the filtering effect of the detector; this effect will be accounted for and discussed below). They are found to be comparable with the experimentally measured ones: 6.7 mm at 0.25 THz, 3.4 mm at 0.5 THz, 2.2 mm at 0.75 THz, and 1.7 mm at 1 THz.

B. 2-D Beam Profile—the Effect of s- and p-Polarized Fresnel Reflection

To further investigate measurement approaches, we simulated all described beam profile scanning methods. First, let us compare the cases where the pinhole was placed at the midpoint of THz setup and the beam was scanned by moving the pinhole alone [see Figs. 1(d) and 2(a)] or by moving pinhole, lens, and detector altogether [see Figs. 1(e) and 2(b)]. To simulate these cases, any radiation outside the pinhole diameter was blocked, and the signal on the detector PCA was estimated as

$$E = \int_{-r}^{r} T_i(x) \cos\left(\theta_t(x)\right) dx \tag{4}$$

where $T_i(x) = \sqrt{1 - R_i^2}$ is the Fresnel transmission coefficient, i denotes the polarization type (p- or s-), and $\theta_t(x)$ is the angle of refraction inside the hemispherical silicon lens. We note that this simulation does not take into account the similar effect at the emitter PCA, responsible for the beam asymmetry observed in Figs. 2–6 and 11. This effect is responsible for a narrowed beam with more pronounced interference lobes in the y direction. $T_i(x) * \cos(\theta_t(x))$ for s- and p-polarizations are shown in Fig. 9(b). In the simulation, T_s and T_p did not demonstrate noticeable difference in THz field profiles. Thus, we plot here in Fig. 9(c)–(j) only the cut along the y-axis corresponding to the s-polarization. Moreover, simulation of the *pinhole-only*, and pinhole, lens and detector scan did not reveal significantly noticeable differences in the beam profile shapes [see Fig. 9(c) and (d)]. Thus, the differences in experimental measurements arise, most likely, due to the difference in Fresnel reflection of s- and p-polarized radiation, that is not fully taken into account in scalar simulations.

To check the origin (e.g., propagation properties or Fresnel reflections) of the difference in beam waist in the results in Fig. 4, simulation of these scanning approaches were performed accordingly, see Fig. 10. From Fig. 10, it can be seen that although the simulation follows the PCA-only scan, the effect of the presence of the lens in measurements involving the pinhole manifests itself differently. In the experiment, it results in a wider beam, while in the simulation it results in a slightly narrower beam, due to the effect of the Fresnel reflection from the TPX lens not accounted for in the simulation.

C. Comparison of Approaches

To obtain a full spatial profile, one must complete a full raster scan of the beam. The simplest approach uses single-aperture scanning, discussed here. A more advanced approach using two-aperture scanning or a mask followed by single-aperture scanning is the Hartmann test. The latter approach has previously been discussed in the context of free-spaced-coupled TDS systems [19], but is not addressed here. The appropriate aperture scanning approach (among those covered here) somewhat depends on the prospective application. The *pinhole and detector* scan provides a more accurate profile of the beam than the *pinhole-only* scan, with less suppression of side-lobes attributed to Fresnel reflections. This conclusion is supported by the ASM results, which show negligible difference between pinhole-only and pinhole and detector movement. For applications where the whole beam is used to perform dielectric property measurements, it is useful to know the excitation region of the sample, and hence a *pinhole and detector* scan would be the profiling method of choice. For applications such as single pixel imaging where the beam is spatially modulated with a series of masks and the "bucket" detector remains stationary, the *pinhole-only* scan provides a pertinent beam waist estimate, with the caveat that it would not be the true value. Thus, the recommended technique would depend on the available time of the users and the application that the characterization is for.

Table II tabulates the beam waist estimates using the different experimental approaches. One can see that the results produced by the knife-edge and pinhole scanning methods are in reasonable agreement. However, the pinhole and PCA scan and both scans without TPX lenses provide much larger beam waist measurements. This is thought to be attributed to the reduced electric field projection in the detector plane for the knife-edge and *pinhole-only* scanning methods. This results in a suppression of the side-lobes, and hence, an underestimation of the beam waist. This understanding is corroborated by the supporting simulations, and we, therefore, conclude that scanning the detector with the pinhole provides a more accurate profile of the beam.

IV. Conclusion

To undertake single pixel imaging measurements, one requires a comprehensive understanding of the beam profile of the imaging system. Here, the beam profile characterization of a commercial all fiber-coupled TDS system in collimated beam configuration is undertaken though a number of profiling techniques. These include the knife-edge method, *pinhole-only* scanning, simultaneous *pinhole and detector* scanning (with and without a TPX lens) and detector scanning without a pinhole or TPX lens. Assisted by stepwise ASM simulations, we unveil the nuances among the different methods that impact the true beam waist estimate. We find that the beam is slightly asymmetric and cannot be considered Gaussian, except when restricted to the central lobe. In the latter instance, the frequency-dependent beam waist ranges loosely from 8.4 mm at 0.25 THz to 2.8 mm at 1 THz. Despite the underestimation of the actual beam waist provided by the *pinhole-only* scan, this would be the most suitable characterization method for single pixel imaging, since the setup is equivalent to the imaging scheme. Our findings also include the 2-D map of the frequency-dependent cross polarized field. We report a moderate cross-polar level (ranging from -11.6 dB to -21.2 dB within the 0.25–1 THz bandwidth), that should be taken into account when dealing with anisotropic materials.

Appendix A
Time-Domain Spectrometer Settings

The all fiber-coupled THz time-domain spectrometer TERA K15 Mark II from Menlo Systems is investigated in this work. Note that its antenna modules are produced by the HHI. The emitter chip is composed of an LT InGaAs/InAlAs on InP multilayer photoconductive antenna ($\approx$0.35 mm thick in total) in a 25 μm stripline configuration, whose radiation is linearly (x-) polarized, and a $\varnothing$6 mm silicon lens [1]. The detector chip is instead a 25 μm dipole antenna with 10 μm gap and a $\varnothing$6 mm silicon lens. Both silicon lenses are substrate-integrated aplanatic hyperhemispherial lenses with 3.5 mm height. The TPX lens has an effective focal length EFL$\approx$54 mm. The THz path is not purged, which restricts the usable bandwidth to 1 THz given the signal-to-noise ratio when using pinholes. The lock-in constant was set to 30 ms and the total temporal length of the recorded waveforms was 52 ps to have a spectral resolution of 15 GHz.

Appendix B
Tabulated Beam Waists

The main lobe beam waists extracted from the different beam profiling approaches discussed in this manuscript are tabulated here in Table II for four different representative frequencies (0.25, 0.5, 0.75, and 1 THz), along with the temporal peak-to-peak beam waist.

Appendix C
Knife-Edge Scan Method

The knife-edge method is a simple technique used to determine beam parameters. Here, a 50 μm thick metallic beam block was translated across the middle plane of the THz setup (whose distance between emitter and detector TPX lenses is approximately 230 mm) in both the x and y directions in increments of 0.5 mm, and the decreasing transmitted electric field measured. From this, the beam waist can be extracted from the derivative of the detected power through Gaussian fitting [45], presented in Table II. The field derivatives presented in Fig. 11(a) and (b) demonstrate the frequency dependent characteristic of the beam waist. These results show that the beam is slightly asymmetric, which is in agreement with other studies for in-house lens-assisted THz systems [16], [18], [21], [31]. Such beam asymmetry results from the combined effect of the slight asymmetric radiation pattern of the feed and polarization dependent Fresnel coefficients at the silicon-air interface. Meanwhile, these results mask the non-Gaussian distribution of the beam that we report in the main text (previously acknowledged in the seminal work on free-space-coupled TDS systems [13]), and thus, the

TABLE II
BEAM WAIST (IN MM) OF THE COLLIMATED THZ TDS BEAM AT DIFFERENT FREQUENCIES AND TIME-DOMAIN PEAK-TO-PEAK BEAM WAIST. THE SCANNED PLANE WAS 115 MM FROM THE EMITTER TPX LENS FOR THE PINHOLE-ONLY SCAN, PINHOLE AND DETECTOR SCAN, AND KNIFE-EDGE SCAN, AND 263 MM (226 MM) FROM THE EMITTER TPX LENS FOR THE SCAN WITHOUT THE TPX LENS AND WITHOUT (WITH) PINHOLE

Freq, THz	Axis	⌀1 mm Pinhole	⌀1 mm Pinhole + PCA	No Pinhole, No TPX lens	⌀1 mm Pinhole, No TPX lens	Knife edge
0.25	X	5.6 ± 0.7	8.4 ± 0.7	13 ± 0.5	10 ± 0.5	6.2 ± 0.3
	Y	5.6 ± 0.7	7.7 ± 0.7	13 ± 0.5	10 ± 0.5	7.4 ± 0.4
0.5	X	3.5 ± 0.7	5.6 ± 0.7	8.5 ± 0.5	6.0 ± 0.5	3.5 ± 0.3
	Y	3.5 ± 0.7	5.6 ± 0.7	8.0 ± 0.5	5.5 ± 0.5	3.4 ± 0.3
0.75	X	2.8 ± 0.7	4.2 ± 0.7	5.5 ± 0.5	4.5 ± 0.5	2.5 ± 0.3
	Y	3.5 ± 0.7	3.5 ± 0.7	5.5 ± 0.5	4.0 ± 0.5	2.0 ± 0.3
1	X	1.4 ± 0.7	3.5 ± 0.7	4.0 ± 0.5	3.5 ± 0.5	1.8 ± 0.3
	Y	1.4 ± 0.7	2.8 ± 0.7	4.5 ± 0.5	3.0 ± 0.5	1.3 ± 0.3
P2P	X	2.8 ± 0.7	4.2 ± 0.7	7.0 ± 0.5	5.5 ± 0.5	3.4 ± 0.3
	Y	2.8 ± 0.7	4.2 ± 0.7	7.0 ± 0.5	5.5 ± 0.5	3.1 ± 0.3

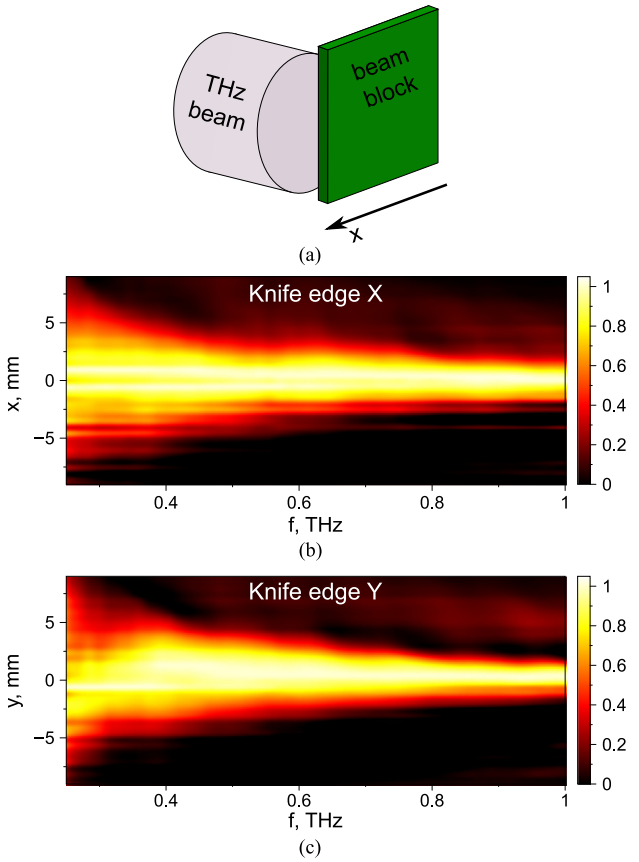

Fig. 11. (a) Knife-edge method illustration, and (b), (c) experimental normalized beam profile spectra obtained from the knife-edge method.

provided beam waist is only a rough estimate of the true beam waist.

APPENDIX D
PCA POLARIZATION SENSITIVITY

To remove the effect of the cross-polar sensitivity of the detector from cross-polar results, electric field measurements were taken for varying rotation angle of the detector with respect to the emitter. The detector was positioned 230 mm from the emitter

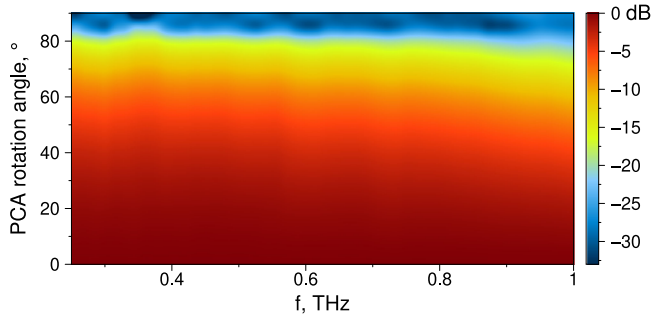

Fig. 12. Polarization sensitivity spectrum of the PCA detector chip.

with a polarizing grid immediately before it, to ensure linear polarization of the incident field. The detector was then rotated around the beam axis (z-axis) from 0° to 90° in increments of 5°, to measure the sensitivity of the detector to rotated polarization. Fig. 12 presents the Fourier transformed field as a function of rotation angle.

A decrease of ∼30 dB is measured from the co-polar to cross-polar measurement across all frequencies. The frequency dependent nonzero field cross-polar measurement was taken into account to correct the registered co- and cross-polar profiles. If we denote the co- and cross-polar PCA sensitivity as $\eta_{\parallel}$ and $\eta_{\perp}$, correspondingly, the measured PCA signals $\tilde{E}_x$ and $\tilde{E}_y$ can be written as

$$\begin{cases} \tilde{E}_x = \eta_{\parallel} E_x + \eta_{\perp} E_y \\ \tilde{E}_y = \eta_{\parallel} E_y + \eta_{\perp} E_x \end{cases} \tag{5}$$

where the actual field values E_x and E_y can be retrieved by solving the system of equations 5 as follows:

$$\begin{cases} E_x = \dfrac{\eta_{\parallel} \tilde{E}_x - \eta_{\perp} \tilde{E}_y}{\eta_{\parallel}^2 - \eta_{\perp}^2} \\ E_y = \dfrac{\eta_{\parallel} \tilde{E}_y - \eta_{\perp} \tilde{E}_x}{\eta_{\parallel}^2 - \eta_{\perp}^2} \end{cases} . \tag{6}$$

This correction method was applied to the experimental data to obtain true values of co- and cross-polarized THz fields presented in Figs. 5 and 6.

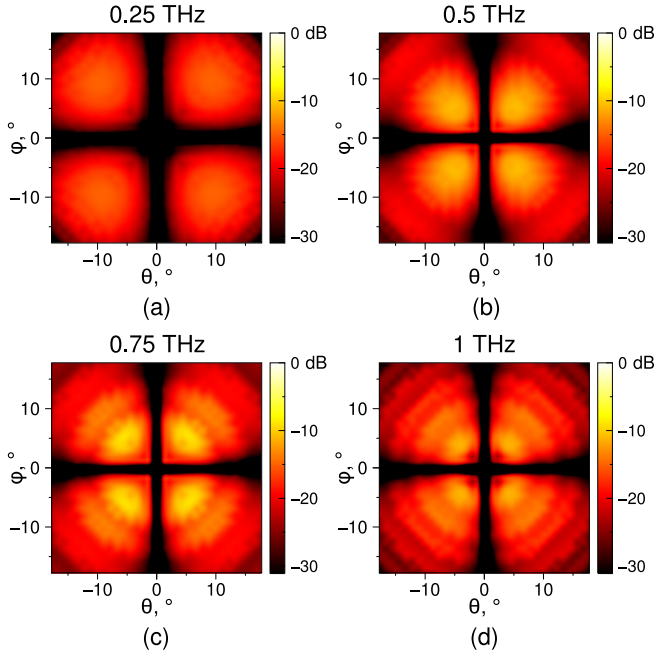

Fig. 13. Far-field cross-polarization THz beam maps simulated in CST Microwave Studio for (a) 0.25, (b) 0.5, (c) 0.75, and (d) 1 THz.

Appendix E
Far-Field Cst Simulations

The transient solver of CST Microwave Studio was used to simulate the response of the emitter chip with the geometrical dimensions given in Appendix A. The stripline and the optical fiber were not modeled to reduce computational effort. The lossless index of refraction of silicon and InGaAs/InAlAs was assumed to be 3.42 and 3.41, respectively. The software-defined discrete port was used to model the emission from the photocurrents as a horizontal short dipole at the bottom edge of the InGaAs/InAlAs substrate. Given the twofold symmetry of the problem, a vertical electric and a horizontal magnetic mirror planes were applied to consider only a quarter of the emitter chip. The software-defined open add space boundary conditions (equivalent to a perfectly matched layer) were used for the simulation box boundaries. Two stopping criteria were considered to either account or not account for the Fabry–Perot effects arising from wave reflections within the Si lens. For the former, the simulation time stopped when the residual energy in the simulation box volume was 60 dB lower than its peak value. For the latter, the simulation time was truncated when the leading pulse exited the simulation box volume. The far-field cross-polarization radiation pattern computed using the temporally truncated simulation is shown in Fig. 13.

Acknowledgment

The authors would like to thank Ms. E. Shalom and Mr. J. Gape for preliminary beam characterization, and A. Gorodetsky also like to thank Magicplot LLC for providing a copy of MagicPlot Pro.

References

[1] G. Carpintero, E. García-Munoz, H. Hartnagel, S. Preu, and A. Raisanen, Eds., *Semiconductor TeraHertz Technology: Devices and Systems at Room Temperature Operation*. Hoboken, NJ, USA: Wiley, 2015.
[2] J. Coutaz, F. Garet, and V. Wallace, *Principles of Terahertz Time-Domain Spectroscopy*. Singapore: Pan Stanford, 2018.
[3] B. B. Hu and M. C. Nuss, "Imaging with terahertz waves," *Opt. Lett.*, vol. 20, no. 16, pp. 1716–1718, 1995.
[4] H. Guerboukha, K. Nallappan, and M. Skorobogatiy, "Toward real-time terahertz imaging," *Adv. Opt. Photon.*, vol. 10, no. 4, pp. 843–938, 2018.
[5] A. Gorodetsky, A. D. Koulouklidis, M. Massaouti, and S. Tzortzakis, "Physics of the conical broadband terahertz emission from two-color laser-induced plasma filaments," *Phys. Rev. A*, vol. 89, no. 3, 2014, Art. no. 033838.
[6] N. V. Petrov, M. S. Kulya, A. N. Tsypkin, V. G. Bespalov, and A. Gorodetsky, "Application of terahertz pulse time-domain holography for phase imaging," *IEEE Trans. Terahertz Sci. Technol.*, vol. 6, no. 3, pp. 464–472, May 2016.
[7] W. L. Chan *et al.*, "A single-pixel terahertz imaging system based on compressed sensing," *Appl. Phys. Lett.*, vol. 93, no. 12, 2008, Art. no. 121105.
[8] R. I. Stantchev *et al.*, "Noninvasive, near-field terahertz imaging of hidden objects using a single-pixel detector," *Sci. Adv.*, vol. 2, 2016, Art. no. e1600190.
[9] M. Naftaly, Ed., *Terahertz Metrology*. Norwood, MA, USA: Artech House, 2014.
[10] P. F. Goldsmith, *Quasioptical Systems: Gaussian Beam Quasioptical Propogation and Applications*. Hoboken, NJ, USA: Wiley, 1998.
[11] M. Camacho, R. R. Boix, S. A. Kuznetsov, M. Beruete, and M. Navarro-Cía, "Far-field and near-field physics of extraordinary THz transmitting Hole-Array antennas," *IEEE Trans. Antennas Propag.*, vol. 67, no. 9, pp. 6029–6038, Sep. 2019.
[12] S. Freer *et al.*, "Revealing the underlying mechanisms behind TE extraordinary THz transmission," *Photon. Res.*, vol. 8, no. 4, pp. 430–439, 2020.
[13] P. U. Jepsen and S. R. Keiding, "Radiation patterns from lens-coupled terahertz antennas," *Opt. Lett.*, vol. 20, no. 8, pp. 807–809, 1995.
[14] F. Garet, L. Duvillaret, J.-L. Coutaz, and M. S. Sherwin, "Evidence of frequency-dependent thz beam polarization in time-domain spectroscopy," in *Proc. SPIE*, vol. 3617, pp. 30–37, 1999.
[15] J. V. Rudd, J. L. Johnson, and D. M. Mittleman, "Cross-polarized angular emission patterns from lens-coupled terahertz antennas," *J. Opt. Soc. Amer. B*, vol. 18, no. 10, pp. 1524–1533, 2001.
[16] J. V. Rudd and D. M. Mittleman, "The influence of substrate lens design in terahertz time-domain spectroscopy," *J. Opt. Soc. Amer. B*, vol. 19, no. 2, pp. 319–329, 2002.
[17] B. Globisch *et al.*, "Fiber-coupled transceiver for terahertz reflection measurements with a 4.5 THz bandwidth," *Opt. Lett.*, vol. 41, no. 22, pp. 5262–5265, 2016.
[18] M. T. Reiten, S. A. Harmon, and R. A. Cheville, "Terahertz beam propagation measured through three-dimensional amplitude profile determination," *J. Opt. Soc. Amer. B*, vol. 20, no. 10, pp. 2215–2225, 2003.
[19] J. F. Molloy, M. Naftaly, and R. A. Dudley, "Characterization of terahertz beam profile and propagation," *IEEE J. Sel. Topics Quantum Electron.*, vol. 19, no. 1, Jan./Feb. 2013, Art. no. 8401508.
[20] J. Klier *et al.*, "Influence of substrate material on radiation characteristics of THz photoconductive emitters," *Int. J. Antennas Propag.*, vol. 2015, 2015, Art. no. 540175.
[21] A. Garufo *et al.*, "Norton equivalent circuit for pulsed photoconductive antennas—part ii: Experimental validation," *IEEE Trans. Antennas Propag.*, vol. 66, no. 4, pp. 1646–1659, Apr. 2018.
[22] K. Elmabruk, K. Demir, H. Altan, A. B. Sahin, and M. Unlu, "Time-domain characterization of the radiation pattern of the terahertz photoconductive antennas," *J. Infrared Millimeter Terahertz Waves*, vol. 40, no. 6, pp. 595–605, 2019.
[23] R. J. B. Dietz *et al.*, "64 μW pulsed terahertz emission from growth optimized InGaAs/InAlAs heterostructures with separated photoconductive and trapping regions," *Appl. Phys. Lett.*, vol. 103, no. 6, 2013, Art. no. 061103.
[24] B. Globisch, R. J. B. Dietz, D. Stanze, T. Göbel, and M. Schell, "Carrier dynamics in Beryllium doped low-temperature-grown InGaAs/InAlAs," *Appl. Phys. Lett.*, vol. 104, no. 17, 2014, Art. no. 172103.
[25] M. Navarro-Cía *et al.*, "Modes in silver-iodide-lined hollow metallic waveguides mapped by terahertz near-field time-domain microscopy," *J. Opt. Soc. Amer. B*, vol. 30, no. 1, pp. 127–135, 2013.

[26] M. Navarro-Cía, M. Vitiello, and C. Bledt, "Terahertz wave transmission in flexible polystyrene-lined hollow metallic waveguides for the 2.5–5 THz band," *Opt. Exp.*, vol. 21, no. 20, pp. 23748–23755, 2013.
[27] M. Navarro-Cía, J. E. Melzer, J. A. Harrington, and O. Mitrofanov, "Silver-coated teflon tubes for waveguiding at 1–2 THz," *J. Infrared Millimeter Terahertz Waves*, vol. 36, no. 6, pp. 542–555, 2015.
[28] A. Podzorov, A. Wojdyla, and G. Gallot, "Beam waist measurement for terahertz time-domain spectroscopy Experiments," *Opt. Lett.*, vol. 35, no. 7, pp. 901–903, 2010.
[29] A. J. Seeds *et al.*, "Coherent terahertz photonics," *Opt. Exp.*, vol. 21, no. 19, pp. 22 988–23 000, 2013.
[30] M. J. Gans, "Cross Polarization in Reflector-Type beam waveguides and Antennas," *Bell Syst. Tech. J.*, vol. 55, no. 3, pp. 289–316, 1976.
[31] A. Neto, N. Llombart, J. J. A. Baselmans, A. Baryshev, and S. J. C. Yates, "Demonstration of the leaky lens antenna at submillimeter wavelengths," *IEEE Trans. Terahertz Sci. Technol.*, vol. 4, no. 1, pp. 26–32, Jan. 2014.
[32] C. Cappellin, P. H. Nielsen, R. Appleby, R. Wylde, and E. Saenz, "Detailed design and RF analysis of a scatterometer for material characterization in the 50–750 GHz range," in *Proc. 12th Eur. Conf. Antennas Propag.*, 2018, pp. 1–5.
[33] M. Neshat and N. P. Armitage, "Terahertz time-domain spectroscopic ellipsometry: Instrumentation and calibration," *Opt. Exp.*, vol. 20, no. 27, pp. 29063–29075, 2012.
[34] C. D. Mosley, M. Failla, D. Prabhakaran, and J. Lloyd-Hughes, "Terahertz spectroscopy of anisotropic materials using beams with rotatable polarization," *Sci. Rep.*, vol. 7, no. 1, pp. 1–9, 2017.
[35] S. A. Kuznetsov, M. A. Astafev, M. Beruete, and M. Navarro-Cía, "Planar holographic metasurfaces for terahertz focusing," *Sci. Rep.*, vol. 5, 2015, Art. no. 7738.
[36] W. Y. Kim *et al.*, "Graphene-ferroelectric metadevices for nonvolatile memory and reconfigurable logic-gate operations," *Nat. Commun.*, vol. 7, pp. 1–6, 2016.
[37] T.-T. Kim *et al.*, "Electrical access to critical coupling of circularly polarized waves in graphene chiral metamaterials," *Sci. Adv.*, vol. 3, no. 9, 2017, Art. no. e1701377.
[38] D. Wang *et al.*, "Photonic Weyl points due to broken time-reversal symmetry in magnetized semiconductor," *Nat. Phys.*, vol. 15, no. 11, pp. 1150–1155, 2019.
[39] A. V. Belashov, M. S. Kulya, N. S. Balbekin, A. Gorodetsky, and N. V. Petrov, "Effect of object thickness on ultrashort pulse diffraction," *Appl. Opt.*, vol. 58, no. 34, pp. 9434–9442, 2019.
[40] C.-T. Tai and C. S. Pereira, "An approximate formula for calculating the directivity of an antenna," *IEEE Trans. Antennas Propag.*, vol. AP-24, no. 2, pp. 235–236, Mar. 1976.
[41] M. Kulya, V. Semenova, A. Gorodetsky, V. G. Bespalov, and N. V. Petrov, "Spatio-temporal and spatiospectral metrology of terahertz broadband uniformly topologically charged vortex beams," *Appl. Opt.*, vol. 58, no. 5, pp. A90–A100, 2019.
[42] V. G. Bespalov and A. A. Gorodetskiĭ, "Modeling of referenceless holographic recording and reconstruction of images by means of pulsed terahertz radiation," *J. Opt. Technol.*, vol. 74, no. 11, pp. 745–749, 2007.
[43] K. Matsushima and T. Shimobaba, "Band-limited angular spectrum method for numerical simulation of free-space propagation in far and near fields," *Opt. Exp.*, vol. 17, no. 22, pp. 19662–19673, 2009.
[44] R. A. Cheville, "Terahertz Time-Domain Spectroscopy with Photoconductive Antennas," in *Terahertz Spectroscopy: Principles and Applications*, S. L. Dexheimer, Ed. Boca Raton, FL, USA: CRC Press, 2008, ch. 1, pp. 1–40.
[45] J. Magnes *et al.*, "Quantitative and qualitative study of gaussian beam visualization techniques," 2006, *arXiv:physics/0605102*.

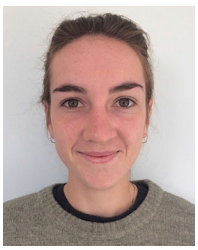

Suzanna Freer received the M.Sc. degree in physics from the University of Sheffield, Sheffield, U.K., in 2018. She is currently working toward a Ph.D. degree in physics with the School of Physics and Astronomy, the University of Birmingham, Birmingham, U.K.

Her current research interests include THz imaging, evanescent fields and spoof surface plasmon platforms.

Andrei Gorodetsky received the B.Sc. and M.Sc. degrees in physics from Saint-Petersburg State University, Saint Petersburg, Russia, in 2003 and 2006, respectively, and the Ph.D. degree in optics from the ITMO University, Saint Petersburg, Russia, in 2010.

Till 2011, he was with the Department of Photonics and Optical Informatics of the ITMO University as Senior Researcher and Assistant Professor. From 2012 to 2013, he was a Postdoctoral Researcher in the Ultrashort Nonlinear Interactions and Sources group at the Institute of Electronic Structure and Laser, Foundation for Research and Technology-Hellas, Heraklion, Greece, where he was engaged in THz metamaterial research and controlled THz generation in two-color plasma filaments. From 2014 to 2016, he was with Optoelectronics and Biomedical Photonics group in Aston Institute of Photonic Technologies, Aston University, Birmingham, U.K. In 2016 and 2017, he was with the Department of Engineering, University of Lancaster, where he was involved in THz electron accelerator development. In 2017–2019, he was with Ultrafast Optoelectronics Group, Department of Chemistry, Imperial College London, developing methods of ultrafast spectroscopy. He is currently with Metamaterials group, University of Birmingham, U.K., and Faculty of Physics and Engineering of ITMO University, St. Petersburg, Russia.

Dr. Gorodetsky is Laureate of Yu. I. Ostrovsky Prize for the best scientific work in the field of optical holography and interferometry in 2012. His main research interests include THz imaging, pump-probe THz studies and development of compact room-temperature THz transceivers.

Miguel Navarro-Cía (Senior Member, IEEE) received the M.Eng. and Ph.D. degrees in telecommunication engineering and M.Res. degree in introduction to research in communications from the Universidad Pública de Navarra, Pamplona, Spain, in 2006, 2010, and 2007, respectively.

From 2006 to 2010, he was a Predoctoral Researcher, FPI Fellowship recipient, with the Department of Electrical and Electronic Engineering, Universidad Pública de Navarra, where he was also a Research and Teaching Assistant from 2010 to 2011. In 2008, he was a Visiting Researcher with the Valencia Nanophotonics Technology Center, Valencia, Spain, for two months. In 2008–2010, he was a Visiting Researcher with Imperial College London, U.K., for four, six and three months, respectively, where he was a Research Associate in 2011 and a Junior Research Fellow from 2012 to 2015. In 2010, he was a Visiting Researcher with the University of Pennsylvania, USA, for three months. In 2012, he was a Research Associate with University College London, U.K. He is currently a Senior Lecturer and a Birmingham Fellow with the School of Physics and Astronomy, University of Birmingham, U.K. He is also a Visiting Researcher with Imperial College London, London, U.K. and University College London, London, U.K. His current research interests include theory, technology and applications of (near-field) time-domain spectroscopy/microscopy/imaging, metamaterials, plasmonics, antennas, and frequency-selective surfaces at millimeter-wave, terahertz, and infrared.

Dr. Navarro-Cía is a Senior Member of the Optical Society of America and a member of the Institute of Physics and the European Optical Society. He was a recipient of the Best Doctoral Thesis in Basic Principles and Technologies of Information and Communications, and Applications corresponding to the XXXI Edition of Awards "Telecommunication Engineers" 2010, the CST University Publication Award (twice) for the best international journal publication using CST Microwave Studio in 2012 and 2016, and the 2011 Junior Research Raj Mittra Travel Grant.